2019

Comparison of the mineralogy of iron ore sinters using a range of techniques

Tom Honeyands
University of Newcastle

James Manuel
CSIRO, james.manuel@csiro.au

Leanne Matthews
University of Newcastle, leanne.matthews@newcastle.edu.au

Damien O'Dea
BHP BILLITON LIMITED

David J. Pinson
BlueScope Steel Limited

See next page for additional authors

Comparison of the mineralogy of iron ore sinters using a range of techniques

Abstract

Many different approaches have been used in the past to characterise iron ore sinter mineralogy to predict sinter quality and elucidate the impacts of iron ore characteristics and process variables on the mechanisms of sintering. This paper compares the mineralogy of three sinter samples with binary basicities (mass ratio of CaO/SiO_2) between 1.7 and 2.0. The measurement techniques used were optical image analysis and point counting (PC), quantitative X-ray diffraction (QXRD) and two different scanning electron microscopy systems, namely, Quantitative Evaluation of Materials by Scanning Electron Microscopy (QEMSCAN) and TESCAN Integrated Mineral Analyser (TIMA). Each technique has its advantages and disadvantages depending on the objectives of the measurement, with the quantification of crystalline phases, textural relationships between minerals and chemical compositions of the phases covered by the combined results. Some key differences were found between QXRD and the microscopy techniques. QXRD results imply that not all of the silico-ferrite of calcium and aluminium (SFCA types) are being identified on the basis of morphology in the microscopy results. The amorphous concentration determined by QXRD was higher than the glass content identified in the microscopy results, whereas the magnetite and total SFCA concentration was lower. The scanning electron microscopy techniques were able to provide chemical analysis of the phases; however, exact correspondence with textural types was not always possible and future work is required in this area, particularly for differentiation of SFCA and SFCA-I phases. The results from the various techniques are compared and the relationships between the measurement results are discussed.

Disciplines

Engineering | Science and Technology Studies

Publication Details

Honeyands, T., Manuel, J., Matthews, L., O'Dea, D., Pinson, D., Leedham, J., Zhang, G., Li, H., Monaghan, B., Liu, X., Donskoi, E., Webster, N. A. S. & Pownceby, M. I. (2019). Comparison of the mineralogy of iron ore sinters using a range of techniques. Minerals, 9 (6), 333-1-333-17.

Authors

Tom Honeyands, James Manuel, Leanne Matthews, Damien O'Dea, David J. Pinson, J Leedham, Guangqing Zhang, Huibin Li, Brian J. Monaghan, Xinliang Liu, Eugene Donskoi, Nathan A.S. Webster, and Mark Pownceby

minerals

MDPI

Article

Comparison of the Mineralogy of Iron Ore Sinters Using a Range of Techniques

T. Honeyands [1,*], J. Manuel [2], L. Matthews [1], D. O'Dea [3], D. Pinson [4], J. Leedham [4], G. Zhang [5], H. Li [5], B. Monaghan [5], X. Liu [1], E. Donskoi [2], N. A. S. Webster [6] and M. I. Pownceby [7]

1 The Australian Research Council (ARC) Research Hub for Advanced Technologies for Australian Iron Ore, University of Newcastle, Callaghan, NSW 2308, Australia; leanne.matthews@newcastle.edu.au (L.M.); xinliang.liu@newcastle.edu.au (X.L.)
2 Carbon Steel Materials Group, CSIRO Mineral Resources, Pullenvale, QLD 4069, Australia; james.manuel@csiro.au (J.M.); eugene.donskoi@csiro.au (E.D.)
3 Principal Technical Marketing, Marketing Iron Ore, BHP, Brisbane, QLD 4000, Australia; damien.p.odea@bhp.com
4 Coke & Ironmaking Technology, BlueScope Steel, ARC Research Hub for Australian Steel Manufacturing, Port Kembla, NSW 2505, Australia; david.pinson@bluescopesteel.com (D.P.); john.leedham@bluescopesteel.com (J.L.)
5 ARC Research Hub for Australian Steel Manufacturing, University of Wollongong, Wollongong, NSW 2522, Australia; qzhang@uow.edu.au (G.Z.); hl762@uowmail.edu.au (H.L.); monaghan@uow.edu.au (B.M.)
6 Team Leader Diffraction Laboratory, CSIRO Mineral Resources, Clayton, VIC 3168, Australia; nathan.webster@csiro.au
7 Geometallurgy Team Leader, Carbon Steel Materials Group, CSIRO Mineral Resources, Clayton, VIC 3168, Australia; mark.pownceby@csiro.au
* Correspondence: tom.a.honeyands@newcastle.edu.au

Received: 30 April 2019; Accepted: 23 May 2019; Published: 28 May 2019

Abstract: Many different approaches have been used in the past to characterise iron ore sinter mineralogy to predict sinter quality and elucidate the impacts of iron ore characteristics and process variables on the mechanisms of sintering. This paper compares the mineralogy of three sinter samples with binary basicities (mass ratio of CaO/SiO_2) between 1.7 and 2.0. The measurement techniques used were optical image analysis and point counting (PC), quantitative X-ray diffraction (QXRD) and two different scanning electron microscopy systems, namely, Quantitative Evaluation of Materials by Scanning Electron Microscopy (QEMSCAN) and TESCAN Integrated Mineral Analyser (TIMA). Each technique has its advantages and disadvantages depending on the objectives of the measurement, with the quantification of crystalline phases, textural relationships between minerals and chemical compositions of the phases covered by the combined results. Some key differences were found between QXRD and the microscopy techniques. QXRD results imply that not all of the silico-ferrite of calcium and aluminium (SFCA types) are being identified on the basis of morphology in the microscopy results. The amorphous concentration determined by QXRD was higher than the glass content identified in the microscopy results, whereas the magnetite and total SFCA concentration was lower. The scanning electron microscopy techniques were able to provide chemical analysis of the phases; however, exact correspondence with textural types was not always possible and future work is required in this area, particularly for differentiation of SFCA and SFCA-I phases. The results from the various techniques are compared and the relationships between the measurement results are discussed.

Keywords: mineralogy; sinter; SFCA; optical point counting; XRD; TIMA; QEMSCAN

1. Introduction

Iron ore sinter remains an important feed for the production of iron and steel, and research continues into the improvement of sinter quality for economic and environmental reasons [1,2].

In the authors' previous paper [3], the mineralogy of an industrial sinter sample was analysed using a combination of reflected light microscopy point counting (PC), automated image analysis (AIA), quantitative X-ray diffraction (QXRD) and electron probe microanalysis (EPMA). It was concluded that the analysis techniques were complementary, with each technique having advantages and disadvantages. In addition, a common set of definitions was agreed upon allowing further collaborative research to be undertaken. One key outcome was the definition of two main types of silico-ferrite of calcium and aluminium (SFCA)—prismatic SFCA (e.g., 60–76 wt % Fe_2O_3, 13–17 wt % CaO, 3–10 wt % SiO_2, 3–11 wt % Al_2O_3 and 0–3 wt % MgO [4]), with blocky and dendritic morphological subtypes, and platy SFCA-I (e.g., 82.6 wt % Fe_2O_3, 13.6 wt % CaO, 1.7 wt % SiO_2 and 2.1 wt % Al_2O_3 [4])—although an absolute alignment between the morphological definition and QXRD relative phase abundances was not possible.

The study of SFCA remains of considerable interest, with a recent paper by Nicol et al. [4] giving an excellent review of work on SFCA phases. SFCA-I and SFCA are stable in discrete compositional ranges and have distinct crystallographic structures, which are presumed to correspond to the platy and prismatic morphologies observed using reflected light microscopy, respectively. However, recent work by Mezibricky and Frolichova [5] has demonstrated that using a morphological approach to distinguishing between SFCA and SFCA-I types is problematic since both phases can exhibit similar textures.

Many authors have reported a difference in the chemical composition of SFCA and SFCA-I [3,6–9]. Compared to SFCA, SFCA-I has a relatively high Fe and low Si composition and has a lower temperature stability range. Tonzetic and Dippenaar [10] used Quantitative Evaluation of Materials by Scanning Electron Microscopy (QEMSCAN) analysis to exploit this difference in chemistry and were able to delineate SFCA-I from SFCA. In their study, SFCA-I was measured as calcium ferrite, as it had levels of silicon and aluminium that were below the detection limit of the QEMSCAN. For SFCA, it was found that a silico-ferrite of calcium (SFC) existed and dominated the SFCA phases and that Mg analogues of SFCA, "aluminates" (SFCAs without iron), silico-ferrites of Na and K and pure silico-ferrites (of a stoichiometry different from pyroxenes or olivines) also existed. Compared with PC and QXRD, significant differences in results were found; for example, QEMSCAN and QXRD reported more SFCA-I than PC, and QEMSCAN reported more hematite than either PC or QXRD.

Given the ongoing uncertainty about the correspondence of morphological and chemical definitions of SFCA and SFCA-I and QXRD results, a round robin test was undertaken using additional sinter samples with a range of binary basicities. The parties involved were the Australian Research Council (ARC) Research Hub for Advanced Technologies for Australian Iron Ores (University of Newcastle, BHP), the ARC Research Hub for Australian Steel Manufacturing (BlueScope Steel, University of Wollongong, and CSIRO Mineral Resources (Clayton, Waterford and Queensland Centre for Advanced Technologies – QCAT laboratories). In this work, the PC, AIA and QXRD were complemented with analysis using the automated scanning electron microscopy (SEM) techniques QEMSCAN and TESCAN Integrated Mineral Analyser (TIMA).

2. Analysis Techniques

2.1. Overview

Three sinter samples with binary basicities (mass ratio of CaO/SiO_2) ranging from 1.7 to 2.0 were circulated to the various laboratories for analysis. Two of these sinter samples were obtained from industrial sinter strands, with the third being produced in a pilot-scale sinter pot. Both a representative sub-sample of crushed sinter and reference polished sections of each sinter were circulated to the laboratories (same polished sections sent to each laboratory in turn). The polished sections were

prepared following the method outlined by Honeyands et al. [3]. Each laboratory used a range of techniques to analyse the different phases in sinter. The techniques used at each centre for sinter mineralogy are summarised as follows:

- University of Newcastle (UON). Sinter mineralogy was analysed by PC and TIMA, and bulk chemical composition and FeO concentration were analysed by XRF and wet chemistry, respectively.
- BlueScope Steel Ltd. (BSL) Port Kembla. Sinter mineralogy was analysed by PC.
- CSIRO Mineral Resources (Clayton, Waterford and QCAT). Sinter mineralogy was analysed by PC, the Mineral4/Recognition4 optical image analysis system, QEMSCAN and QXRD.
- University of Wollongong (UOW). Sinter mineralogy was analysed by image analysis.

The bulk chemical compositions of the samples are given in Table 1.

Table 1. Average bulk chemical analysis determined by XRF and wet chemistry for the sinter samples (wt %).

Analyte	UN011 (Plant)	UN154 (Plant)	UN016 (Pot)
Fe total	57.38	56.73	56.87
Fe^{2+}	5.45	5.91	4.45
SiO_2	5.56	5.43	4.95
Al_2O_3	1.80	1.87	1.73
P	0.06	0.07	0.05
CaO	9.24	10.04	9.83
MgO	0.95	1.76	1.79
Basicity (CaO/SiO_2)	1.66	1.85	1.99

2.2. *Reflected Light Microscopy–PC*

PC under a reflected light microscope is a well-established method used to characterise sinter mineralogy. The PC in this study was carried out following the scheme described by Honeyands et al. [3], which included identification of:

- primary hematite
- secondary hematite
- magnetite
- platy SFCA-I
- prismatic SFCA, including morphological subtypes blocky and dendritic
- dicalcium silicate (C2S)
- glass

PC of sinter mineralogy was carried out using a stepping stage, mounted on the stage of the microscope, with an eyepiece graticule for location. PC was carried out at a magnification of 200× by all laboratories except BlueScope Steel, who used a magnification of 400×. The step size was set up to obtain a statistically representative data set, ideally covering the whole surface of the polished mount in case of any distribution bias (e.g., particle size, density segregation), introduced during mount preparation. Each point was counted within a designated category and no data were recorded if the graticule intersecting crosshairs were located outside the boundary of a sinter particle. A consistent technique was normally applied in cases where the crosshairs intersected the boundary between two or more phases, in which the phase occupying a selected quadrant (i.e., left upper, left lower, right upper, right lower) immediately adjacent to the intersecting crosshairs was then recorded. The stepping stage may be controlled by a manual PC unit, which also records the data, or by a computer keyboard via an interface with data logging software, with direct entry of data into a spreadsheet. Typically, between 500 and 2000 points were counted per sample.

2.3. Automated Image Analysis (AIA)

At University of Wollongong, the whole polished section of the reference sample was imaged at a magnification of 200× using a Leica DM6000 optical microscope (Wetzlar, Germany). Up to 3125 individual images were taken automatically, grouped into 12 images and then processed by the software Leica Application Suite V4.0 to obtain the volumetric percentages of hematite, magnetite and total SFCA. Due to the limitations of the software, the sum of SFCA and SFCA-I and total content of primary and secondary hematite were obtained, whereas C2S could not be distinguished from pores.

CSIRO has developed the software Mineral4/Recognition4, which has the capability to identify different textures of the same mineral using a textural identification routine [11,12]. Recently this capability has been applied to segment different morphologies of the same mineral in sinter characterisation [13]. To characterise the sinter samples, the whole polished section surface was imaged at a magnification of 200×. Altogether, up to 200 MosaiX (Carl Zeiss Microimaging GmbH, Göttingen, Germany) images were collected, where each image contained 4 × 4 (16) elementary images. The average size of each MosaiX image was 4500 × 3600 pixels, with a scaling factor of 0.53 mm/pixel (i.e., an area of approximately 2.38 × 1.9 mm). The system was calibrated using a cubic zirconia reflectivity standard prior to imaging.

2.4. Quantitative X-ray Diffraction

At CSIRO Clayton, approximately 4 g of the coarsely ground sinter was micronised in a McCrone micronising mill (Westmont, IL, USA) under ethanol (4 min·g^{-1}) to reduce the particle size to that suitable for QXRD analysis (≈10 µm). Diffraction data were collected on the centrifuged and dried sample, from 5 to 140° 2θ using a PANalytical MPD instrument (Almelo, The Netherlands) fitted with a cobalt long-fine-focus X-ray tube operated at 40 kV and 40 mA. The incident beam path was defined using 0.04 radian Soller slits, a 20 mm mask, a 0.5° fixed divergence slit and a 1° anti-scatter slit. The diffracted beam incorporated a second set of Soller slits, a graphite monochromator to eliminate unwanted wavelengths and a 4.6 mm anti-scatter slit. An X'Celerator detector (Almelo, The Netherlands) was used in scanning line (1D) mode with an active length of 2.122° 2θ and a step size of 0.0167° 2θ. Crystalline phase identification was carried out using X'Pert HighScore Plus (Almelo, The Netherlands) [14].

Quantitative phase analysis was achieved using the Rietveld method [15] with the software TOPAS V5 (Bruker AXS, Madison, Wisconsin, USA [16]). The crystal structure information used as the basis for the refinement was taken from Blake et al. [17] for hematite, Hamilton [18] for magnetite, Hamilton et al. [6] and Liles et al. [19] for SFCA and Tsurumi et al. [20] for C2S. The Rietveld method directly reports the relative weight fractions of all crystalline phases included in the model, which thus sum to 100%; the approach taken here to calculate the absolute weight fractions and thus also the amorphous/unidentified phase content was a traditional external standard approach [21], using corundum (Baikalox Regular product—CR1, Baikowski, Charlotte, NC, USA) as the external standard.

2.5. Scanning Electron Microscopy (SEM)

In preparation for SEM examination, the polished sections were coated with a 15 nm thick carbon film prior to analysis by the electron beam instrument. The coating of carbon was necessary to prevent charge build-up on the sample during subsequent analysis. Two types of analyses were conducted: QEMSCAN and TIMA. Both of these methods are under development for the analysis of iron ore sinter minerals, and further refinement of the results is expected in future work.

2.5.1. QEMSCAN

A QEMSCAN species identification protocol (SIP) file [22] is being developed for sinter mineralogical analysis by CSIRO and was applied in the analysis of the three samples used in

this study at CSIRO's Waterford laboratory. The samples were mapped using the particle mineral analysis mode at an accelerating voltage of 25 keV and a beam current of 5 nA with a tungsten filament source. The area mapped used a beam step size of 5 µm, corresponding to a grid with points spaced every 5 µm horizontally and vertically across the sinter particles, with 1000 counts collected per analysis point. The map conditions were selected to give the best compromise between covering a large area of the representative particle within a reasonable timeframe (<10 h per analysis) while at the same time providing sufficient textural and chemical resolution to resolve the detail of the mineralogical phases present.

2.5.2. TIMA

TIMA is also an automated scanning electron microscopy system that has been used in multiple industries. The TIMA system at UON is comprised of the TIMA hardware and Version 1.5.50 TIMA software. Featuring four energy-dispersive X-ray (EDX) detectors attached to the large chamber of the VEGA (thermionic emission—tungsten) platform, the system is capable of three types of analysis (Modal, Liberation and Bright Phase Search) with different acquisition modes (High-resolution mapping, Point spectrometry, Line mapping and Dot mapping) [23].

After building the sinter mineralogy library and comparing the results of the different analysis modes, liberation analysis using the high-resolution mapping mode was chosen for this study. A 15 keV accelerating voltage, 4.76 nA probe current and ≈18.20 beam intensity were selected for the analysis operation. To give a better mineral classification, the scans were set up at 15 mm working distance with a 4 µm pixel size (resolution) having a field size of 500 × 500 µm and the value for separation of phases was 17. The samples were Ø30 mm in diameter and the analysed area was Ø26 mm (2025 fields) for each sample due to the edge effects. The total scan for one sample was around 14 h with approximately 4000 counts collected per analysis point.

All optical and SEM-based microscopy was carried out on the same polished sections, over the entire area of the sample, unless otherwise noted. Polished sections were prepared from <2 mm crushed, representative product sinter samples, which were longitudinally sectioned and re-mounted to overcome any density-/size-related settling bias. The whole area of the sample was analysed unless otherwise specified.

3. Sinter Mineralogy Results

3.1. Reflected Light Microscopy

The same mounted and polished sinter samples were analysed at each of the laboratories using reflected light microscopy techniques. The sinter phases referred to in this paper were defined previously by Honeyands et al. [3]. An example of a photomicrograph showing the key morphological distinction between prismatic SFCA and platy SFCA-I is given in Figure 1. Primary (H-prim) and secondary hematite (H-sec) are also shown.

The results of both PC and AIA are presented in Figure 2a–c. Generally, there is an increase in the proportions of SFCA and SFCA-I as the binary basicity of the sinters increases, with a resulting decrease in the total iron oxide and glass concentration. The magnetite level also decreased as the basicity increased; however, the magnetite concentration of UN016 is approximately half the magnetite content of the other two samples. UN016 was produced in a sinter pot, whereas the other sinters were from industrial sinter strands, and the different sintering conditions experienced by the pot sinter may have influenced the magnetite concentration.

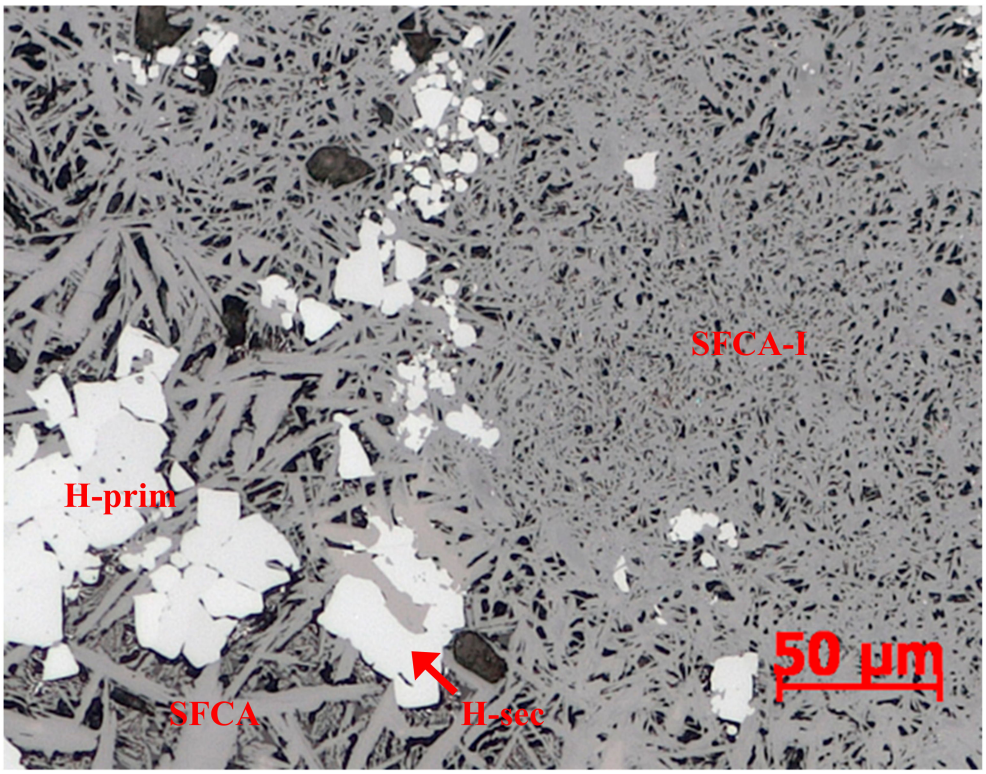

Figure 1. Reflected light photomicrograph showing typical occurrence of silico-ferrite of calcium and aluminium (SFCA) morphological types plus primary and secondary hematite in an iron ore sinter (UN016).

Agreement between the different laboratories is generally acceptable, although higher differences occur for UN011 sample (see Table 2). The variability in SFCA, primary hematite, secondary hematite and magnetite for UN011 were all higher than 12%. The variability in SFCA, magnetite and total hematite concentration for UN154 and UN016 samples was no more than 11%. Significant variability was found in the SFCA-I concentration for all three samples, but the variation decreased as the amount of this phase increased in the sample.

Table 2. Mean result of optical AIA and PC results (area %), and relative standard error (1 standard deviation divided by the mean result).

	UN011 Average	UN011 SE	UN154 Average	UN154 SE	UN016 Average	UN016 SE
Primary Hematite	19.4	24	7.1	25	14.9	13
Secondary Hematite	22.1	17	17.6	6	18.8	15
Total Hematite	41.5	5	24.7	6	33.7	9
Magnetite	31.7	12	32.0	7	13.2	11
SFCA-I	1.0	44	1.8	54	6.2	28
SFCA	15.1	17	32.0	7	37.5	7
C2S	2.6	44	6.4	20	4.2	55
Glass	3.9	6	5.7	23	2.8	50

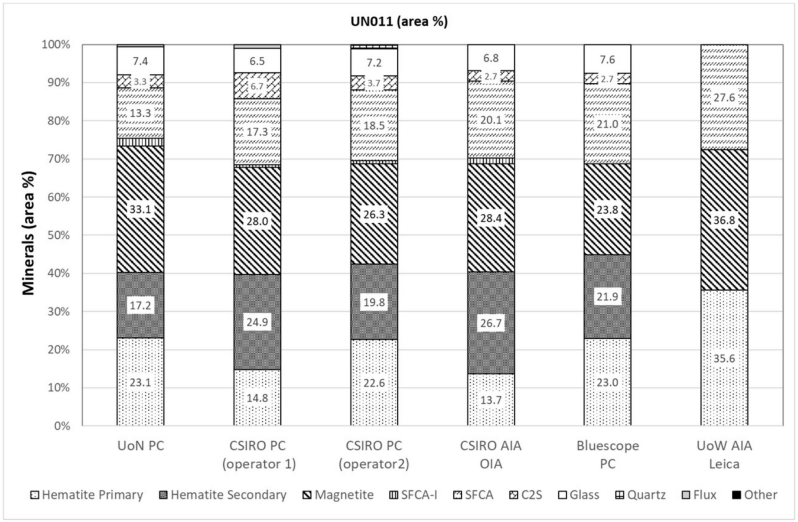

(**a**)

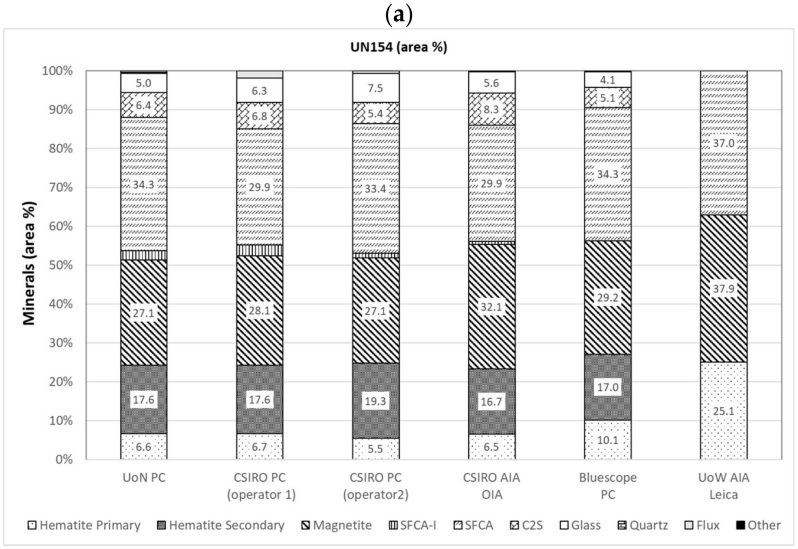

(**b**)

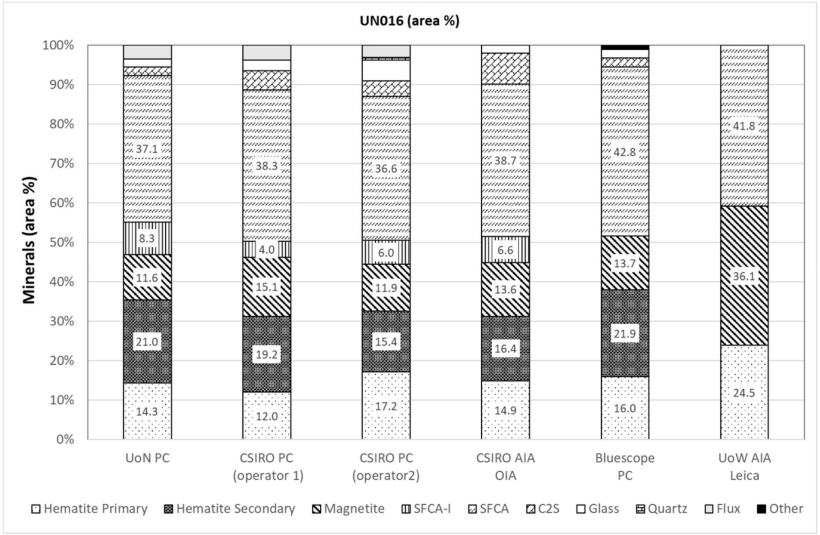

(**c**)

Figure 2. Results of point counting (PC) and automated image analysis (AIA) from reflected light microscopy for the three sinter samples: (**a**) UN011, (**b**) UN154 and (**c**) UN016. N.B. The "flux" category includes calcined limestone/dolomite and unreacted aluminosilicate gangue.

There is also significant variation in the results between laboratories for C2S and glass. C2S is known to be problematic, as this phase is water soluble and can be removed during polishing of the sample [24]. This leaves the mineralogist with the task of interpreting the shape of pores in the polished section as evidence of the presence of C2S.

3.2. Automated Image Analysis (AIA)

The use of AIA is expected to have the advantages of being operator independent and having a higher spatial resolution than the PC- and SEM-based measurements. However, the analysis system needs to be able to distinguish the desired phases and textures.

The University of Wollongong used the Leica Application Suite V4.0 to perform AIA of the sinter sample. This analysis utilised thresholding of the greyscale levels in images to distinguish total hematite, magnetite and total SFCA. Although the method has limitations in identifying some subcategories of mineral phases, it provides a quick and efficient measure for quantitative phase analysis of sinter samples satisfying general sintering research requirements. The total SFCA results for all three samples using the simple thresholding performed at the University of Wollongong are approximately consistent with the PC results shown in Figure 2.

Further techniques are required to segment primary from secondary hematite, SFCA from SFCA-I, and C2S from glass, as these phases have overlapping greyscale ranges. Mineral4 uses a textural identification algorithm to resolve these different morphologies. Figure 3 gives good examples of SFCA-I and different SFCA textures. Figure 3a is a reflected light photomicrograph (MosaiX image) and Figure 3b is the associated mineral map using CSIRO's AIA system. This image was chosen to show all of the identified phases, including SFCA-I. In Figure 3, SFCA is mainly associated with magnetite, whereas SFCA-I is localised in occurrence and mostly associated with primary and secondary hematite.

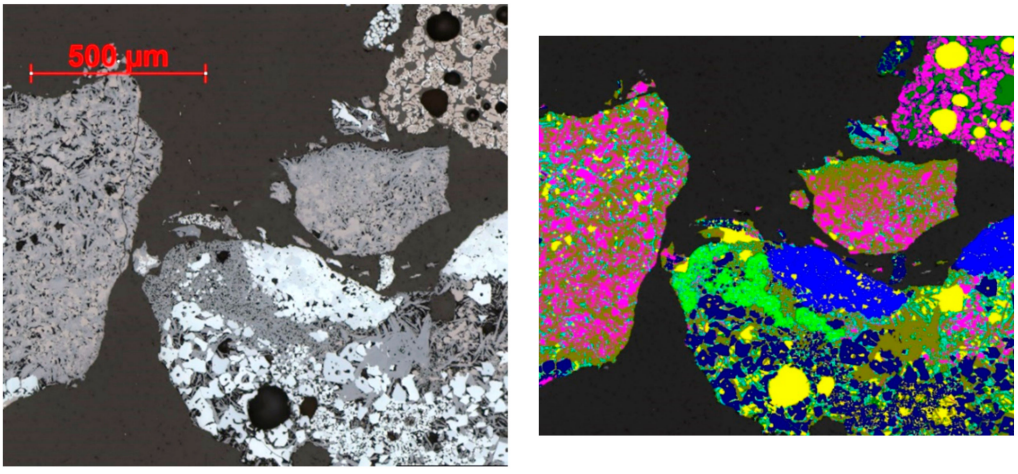

(**a**) (**b**)

Figure 3. (**a**) Typical reflected light microscopic image (MosaiX image) from sample UN154 and (**b**) mineral map obtained during AIA using CSIRO's AIA system: primary hematite—light blue, secondary hematite—dark blue, magnetite—magenta, platy SFCA I—light green, prismatic SFCA—olive, glass—dark green, C2S—cyan, open porosity and epoxy within particles—yellow.

The recognition/identification of different phases by Mineral4 was calibrated to match the phase identification used by CSIRO mineralogists, without prior reference to PC results. The results obtained are very close to the operator 1 PC results overall; however, the system is flexible and could be tuned differently if desired.

3.3. Quantitative X-Ray Diffraction

The final Rietveld fit to the QXRD data collected for the sinter samples is shown in Figure 4. Based on the pattern fit, the calculated values (wt %) for the phases in the samples are provided in Table 3. Using the external standard, the amorphous concentration of the samples was quantified. As a first approximation, the amorphous concentration in the samples was assumed to correspond to glass.

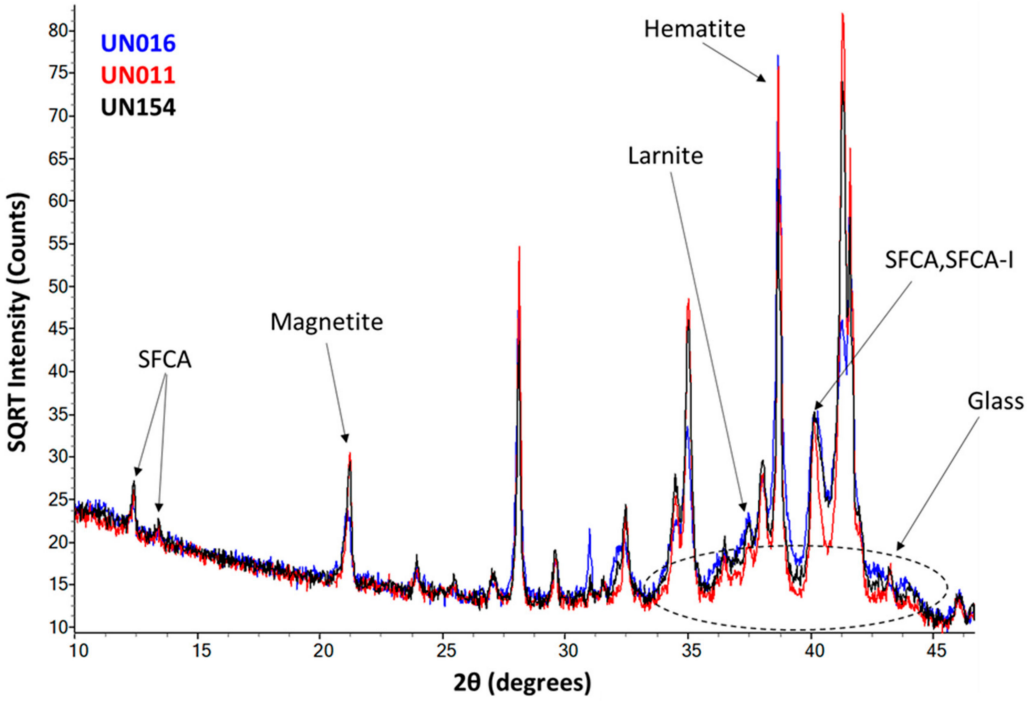

Figure 4. Overlay of XRD patterns (λ = 1.789 Å) collected for the UN011, UN154 and UN016 samples. Peaks from major phases—hematite, magnetite, SFCA, SFCA-I, larnite (C2S) and glass—are labelled. The dashed oval highlights the broad hump between ≈ 33 and 45° 2θ from the amorphous material (glass). SQRT—square root.

Table 3. Quantitative X-ray diffraction QXRD results for the sinter samples (wt %). N.D—not detected.

Mineral	UN011 (Plant)	UN154 (Plant)	UN016 (Pot)
Hematite	38.2	30.0	40.0
Magnetite	29.8	27.5	12.0
SFCA-I	N.D.	N.D.	11.0
SFCA	17.4	22.3	14.0
C2S	6.6	6.2	6.0
Mordenite	N.D.	N.D.	0.5
Quartz	N.D.	N.D.	0.5
Glass (amorphous)	8.0	14.0	16.0
Total	100.0	100.0	100.0

Although XRD generally offers advantages in quantifying mineral phases, there are advantages and disadvantages for characterising iron ore sinters. The primary disadvantage is that XRD cannot distinguish phases that can be further refined on the basis of texture (e.g., primary hematite, secondary hematite and the various textural forms of SFCA). In the case of hematite, there is no obvious solution and hence XRD only provides a total hematite concentration (i.e., a sum of the primary and secondary hematite content), whereas the optical results are able to provide a more refined discrimination of these two textures. The optical mineralogy results cannot be directly compared to the XRD results as they are measured on an area % basis. Assuming a certain density for each phase (hematite 4.9, magnetite

5.1, SFCA 3.8, SFCA-I 3.4, glass 2.5, all others 3.1 kg/m^3), the results can be converted into wt % and the resulting comparison is shown in Figure 5 for the mean results of PC and CSIRO's AIA.

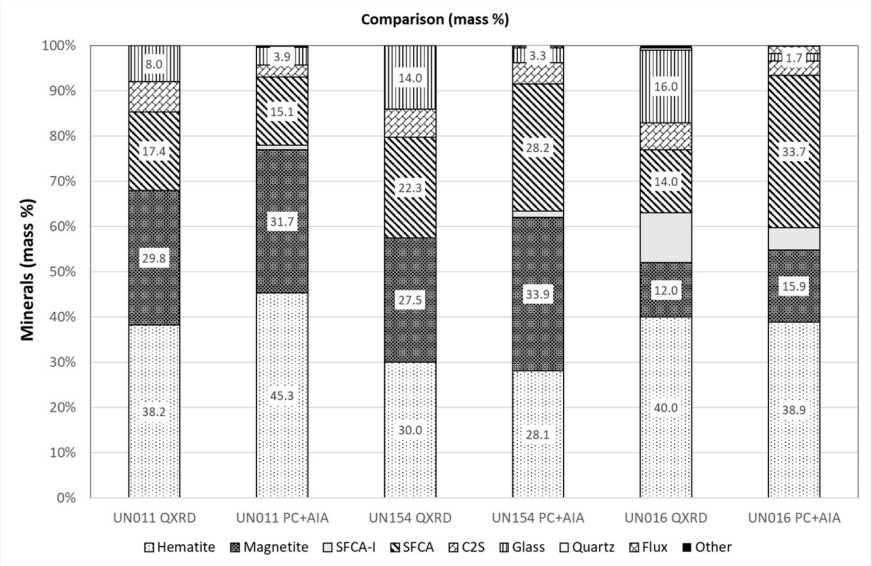

Figure 5. Comparison of QXRD and reflected light microscopy results (average of all PC and image analysis results except University of Wollongong (UOW) results) for the three sinter samples.

As shown in Table 3 and Figure 5, the total hematite concentration measured using XRD and PC matches each other for the UN154 and UN016 samples, but is lower in the XRD data than in the point count for UN011. The magnetite concentration in the UN154 and UN016 samples is slightly overestimated by PC compared to XRD. Uncertainty in the density assumed for magnetite when converting from area % to mass % for the PC results may have contributed to this. It is also notable that with the exception of UN016, the magnetite concentration determined by both techniques is higher than that consistent with the Fe^{2+} content of the sinter determined by XRF chemical analysis.

Hamilton et al. [6] and Mumme et al. [7] demonstrated that SFCA and SFCA-I have different crystalline structures and hence produce significantly different XRD patterns, which can be used to uniquely identify and quantify their amounts in sinter. In the authors' previous paper [3], the total SFCA measured in the sample using XRD and PC matched quite well. In this work, it appears that the XRD technique underestimates the total level of SFCA for the higher basicity sinter samples. However, the amount of glass identified in the XRD results is clearly higher than that measured by PC. Glass cannot be determined directly by XRD due to its lack of crystalline structure, and in this study the amount of glass in the samples was estimated using the amount of amorphous material calculated to be present. This can potentially result in an overestimation in the total glass content, especially if other fine-grained amorphous material is present.

The higher basicity UN016 sample (binary basicity 2) had a higher fraction of SFCA-I as determined by both QXRD and PC. This is consistent with XRD data which show that higher basicity stabilises SFCA-I [25]. It has been assumed that prismatic and platy SFCA correspond to SFCA and SFCA-I, respectively, but based on this evidence, it appears that PC is under-representing the proportion of SFCA-I present. Traditionally, morphologies are used to distinguish these two variants when using optical-based techniques; however, recent work by Mezibricky and Frolichova [5] has demonstrated that using a morphological approach to distinguish between SFCA and SFCA-I types is problematic since both phases can exhibit similar textures.

Finally, the C2S concentration is systematically lower in PC compared to XRD. As discussed earlier, this is expected as the C2S tends to be removed during re-polishing to re-carbon coat the samples and also implies that it is, in some cases, being mis-identified as porosity.

It is notable that in both the high basicity samples, the increased amorphous content occurs at the expense of magnetite and SFCA. One potential explanation for this observation is the existence of a poorly crystalline intermediate or transitional phase at the interface between magnetite and SFCA.

3.4. SEM

Given the difficulty in reconciling all mineral phases in the sinter sample by PC and QXRD, in particular the different textural types of SFCA, two different SEM-based approaches were used to examine a number of the key morphologies present. SFCA has been found to be stable on the $CaO{\cdot}3Fe_2O_3$-$CaO{\cdot}3Al_2O_3$-$4CaO{\cdot}3SiO_2$ (CF3-CA3-C4S3) plane [9,26,27]. Murao et al. [27] determined thermodynamic stability for SFCA, and this range is reproduced in Figure 6. Less work has been reported for SFCA-I; however, many authors have reported a difference in the chemical composition of SFCA and SFCA-I [3,5,7,28]. Selected results are plotted in Figure 6 for comparison. Based on this, it is hypothesised that SFCA-I plots toward the CF3-CA3 axis.

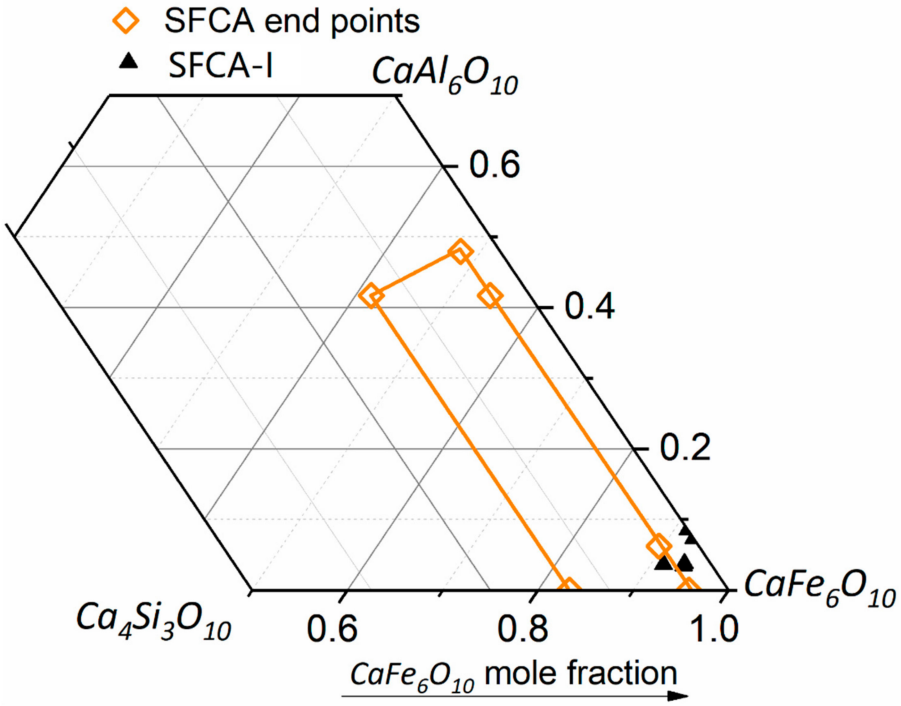

Figure 6. Compositions of the six end members of the SFCA solid solution by Murao et al. 2018, along with published compositions for SFCA-I [3,4,7,28].

3.4.1. QEMSCAN

An example of the QEMSCAN phase mapping results obtained from a sinter particle containing both prismatic and platy SFCA morphologies is presented in Figure 7 with particle mineral maps acquired at higher and lower resolution, to highlight phase boundary effects and the fine-scale intergrowth of the sinter mineralogy phases. Ca-ferrite/SFCA sub-categories were discriminated, based on the dominant presence of Ca and Fe in individual EDX spectra, as well as the less common and minor presence of Si and/or Al. As shown in Figure 7b, the dominant ferrite phase ("CF1") largely corresponds with prismatic SFCA identified optically (Figure 7a), whereas the finely intergrown platy SFCA-I is recognised as "CF2".

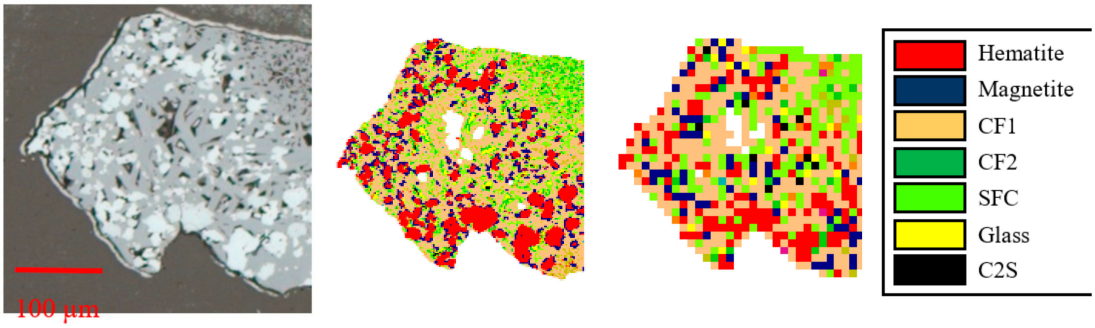

(**a**) (**b**) (**c**)

Figure 7. Comparison of (**a**) the optical photomicrograph and (**b**) the corresponding Quantitative Evaluation of Materials by Scanning Electron Microscopy (QEMSCAN) image at (**b**) 2 µm and (**c**) 10 µm pixel resolution, of a sinter particle colour-coded as hematite—red, magnetite—blue, prismatic SFCA (CF1)—tan, platy SFCA-I (CF2)—dark green, with SFC—light green, minor interstitial glass—yellow and C2S—black. N.B. Magnetite appears as a phase boundary artefact in this image; QEMSCAN discrimination of prismatic and platy SFCA types is approximate. N.B. Remnant carbon coating is visible at the interface between the particle edge and mounting resin in (**a**).

The majority of SFCA was found to have zero or negligible levels of silicon and aluminium in individual point analyses, but was recognised from a "calcium ferrite" composition, sub-divided into CF1 and CF2 in Figure 7. The discrimination was based on an Fe-count threshold in the individual EDX spectra. As shown in Figure 7b, the dominant ferrite phase ("CF1") corresponds reasonably well with prismatic SFCA identified optically (Figure 7a), whereas the finely intergrown platy SFCA-I is more commonly recognised as "CF2". The typical lack of Si and Al in the EDX spectra of ferrite phases is thought to be due to limited resolution from the relatively low count rate (1000 counts) used for individual analysis points, given the relatively low proportions of Al and Si present in SFCA. In terms of composition, the higher Fe content of CF1, compared with CF2, is the opposite relationship to that expected from Figure 6. This effect reflects similar observations made by Tonzetic and Dippenaar [10], although the relative proportion of "calcium ferrite" phases appeared to be higher in the current results, compared with "SFC" (Ca-ferrite with a significant Si count) or "SFCA" compositions, where a significant level of both Si and Al was present. In terms of composition however, the higher Fe content of CF1, compared with CF2, is the opposite relationship to that expected from Figure 6. The "SFC" phase appears to represent, at least in part, a boundary phase between SFCA and interstitial glass/C2S.

All Ca-ferrite/SFCA subtypes have been combined as total SFCA in the modal abundance comparison plots in Figure 9. The composition of the phases is being further investigated with detailed electron microprobe analysis, which should help to resolve some of the apparent anomalies in phase identification outlined above. Minor Si-bearing ("SFC", light green in Figure 7b) and localised Si, Al-bearing ("SFCA") ferrites were also recognised, which were grouped with prismatic SFCA. These were mainly associated with the boundary between SFCA and areas of Si-rich glass, or occurred adjacent to localised aluminosilicate gangue associated with Fe-oxides, as apparent reaction rims. Hematite and magnetite had overlapping Fe:O ratios and backscattered-electron intensity, somewhat dependent on mineralogical association and due to phase boundary and particle edge effects, and were therefore discriminated on the basis of minor element concentration. The calibration between the Fe-oxides was sensitive, but the resulting discrimination corresponded reasonably well to magnetite and hematite recognised from optical microscopy. Discrimination between hematite/magnetite and SFCA/SFCA-I was influenced by phase boundary overlap, evident in Figure 7b,c. This occurred due to pixel overlap at actual boundaries between phases at the sample surface (e.g., magnetite identification at the boundary of hematite grains and SFCA) and due to interaction volume (up to several μm^3, depending on phase density) of the electron beam with the sample.

Overall, the QEMSCAN results compared reasonably well with those obtained from other microscopic methods. The ratio of Fe-oxides to SFCA in UN154 was relatively high, but for this sample, unlike UN011 and UN016, the full vertical thickness of the section was not analysed due to beam failure during the run. This may explain the anomaly, due to potential bias from preferential settling of particles during mounting. The proportion of C2S was low, but this is likely to be affected by dissolution during section preparation, as noted above. C2S was detected from exposed material below the surface of the polished mounts, but was likely to be under-represented for this reason, due to boundary effects. The "flux" category included Al, Si-rich gangue associated with Fe-oxides and calcined limestone/dolomite (Ca/Mg-rich, but low Fe, Si) areas. The "Other" category included some debris within larger open pores, detected from below the surface of the mounts.

3.4.2. TIMA

A mineral library was developed for the TIMA using a range of well-characterised pot and plant sinter samples. TIMA is designed for fast automated analysis of mineral samples; however, this requires some compromises between speed and accuracy of analysis.

The interaction volume for the electron beam is approximately 1.5 µm, resulting in some difficulty in analysis of very fine textures such as SFCA-I, and for the boundaries between phases, although the 15keV accelerating voltage would be expected to improve this for the TIMA results. In addition, the initial segmentation of the sample based on backscattered electron level may need further refinement in future work. As a result, distinguishing SFCA and SFCA-I on the basis of chemical composition such as Fe content [4], Si content or Fe/Si ratio as anticipated above was not possible. It was also not possible to distinguish hematite from magnetite, due to the very similar backscattered-electron signal from the two phases. Figure 8 shows a comparison of the backscattered-electron (BSE) image and TIMA liberation analysis results, which proves TIMA is able to accurately differentiate iron oxides from other minerals.

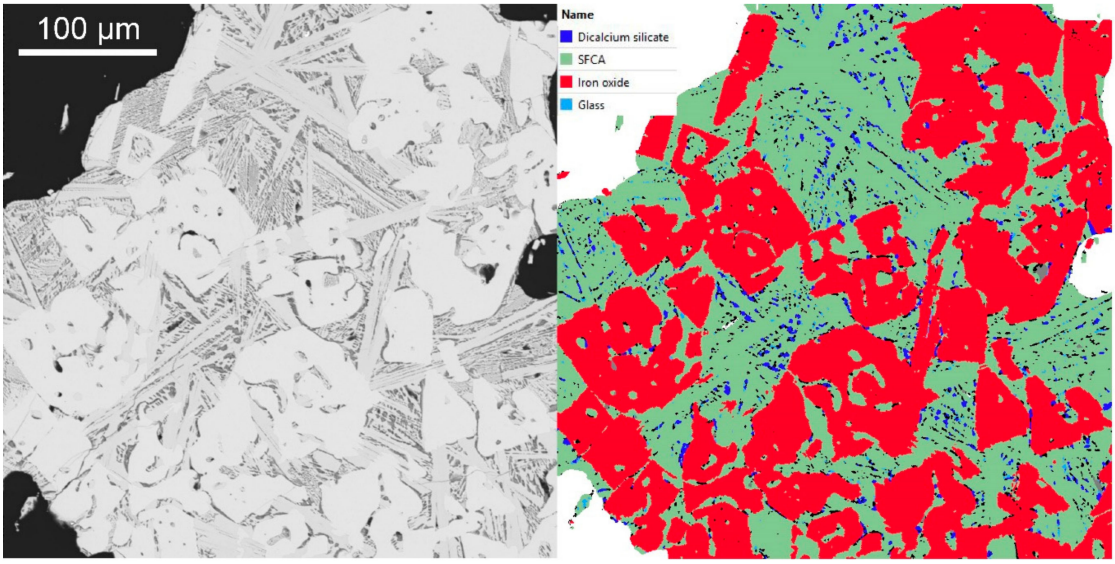

Figure 8. Comparison of backscattered-electron (BSE) and liberation analysis images: iron oxide—red; SFCA—turquoise; C2S—blue; unclassified—black.

3.5. Comparison of Modal Abundance Data from Different Techniques

Results of QEMSCAN (marked as QS) and TIMA analysis (measurement: liberation analysis, scanning mode: resolution) are compared with XRD and PC data in Figure 9. Hematite and magnetite are combined as total iron oxide and SFCA-I and SFCA have been similarly combined. The total iron oxide concentration measured by TIMA agreed well with the total iron oxide measured by PC

and QXRD with the difference less than 5%; the total SFCA amounts determined by TIMA were all relatively lower (the differences were no more than 6%) than the PC results, lending some weight to the hypothesis that some amorphous SFCA phases may exist in the sinter samples.

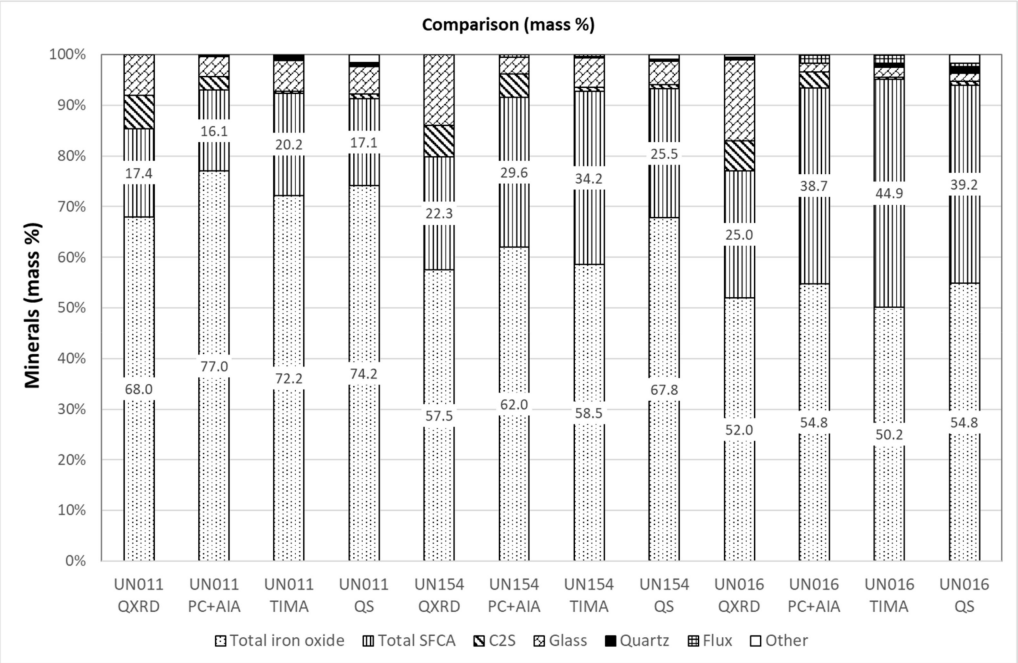

Figure 9. Comparison of QXRD, PC, QEMSCAN and TESCAN Integrated Mineral Analyser (TIMA) results for the three sinter samples.

Although differences existed among different techniques, all results show decreasing Fe-oxide concentration and increasing SFCA fraction with increasing basicity. The amounts of glass identified in the optical and SEM quantitative mineralogy results are similar for UN011 and UN154, but significantly lower for the high basicity pot grate sinter, UN016. In contrast, UN016 has the highest amorphous content determined by XRD, followed by UN154. This provides clear evidence that XRD amorphous content does not directly correlate with glass content (and may in fact show an inverse correlation) for these three sinter samples.

C2S concentration is relatively constant and consistently higher in the XRD results than in PC, and very low in the SEM-based techniques. No clear trend in C2S content is evident between the three samples, although it is likely that the lower amounts determined from microscopic techniques reflect partial loss due to dissolution during section preparation, as noted above. The ratio of glass to C2S content is consistently higher in the results from SEM-based analysis than from PC.

Further work is needed to understand what other components may be contributing to XRD amorphous content. Possible candidates include poorly crystalline SFCA and magnetite. The relative over-representation of both magnetite and prismatic SFCA in PC results increases with increasing XRD amorphous content from UN011 to UN016 (Figure 4). It is not, therefore, a simple case of incorrect (or operator-dependent) discrimination between magnetite and SFCA under the microscope, although this may help to explain variation between individual point counts (Figure 2).

In terms of overall sinter characteristics, the relatively high SFCA-I and low magnetite contents of UN016 suggest lower temperature and/or more oxidising conditions compared with UN154. The higher proportion of primary hematite, low glass content (from microscopy) and greater retention of remnant flux particles are also consistent with lower sintering temperature. The low basicity UN011 sinter also has relatively high primary hematite content, but formed considerably less SFCA, suggesting less assimilation of Fe-oxides due to lower availability of Ca. The much higher SFCA-I concentration

measured by XRD for UN016, compared with PC, suggests that SFCA-I also occurs in a different morphological form than the finely intergrown texture typically recognised (Figure 1).

4. Conclusions

Three different iron ore sinter samples with binary basicity (mass ratio of CaO/SiO_2) between 1.7 and 2.0 were analysed using a number of different techniques, with each providing different and generally complementary information about the mineralogy and texture of the sinter.

PC under reflected light microscopy was able to distinguish a range of mineralogical and textural types, including primary and secondary hematite, magnetite, C2S and glass. It is now possible to automate PC using systems such as Mineral4/Recognition4 and to eliminate subjectivity associated with individual mineralogists, providing calibration can be effectively set up and benchmarked against reference data.

QXRD was used to quantify the bulk mineralogy of the sample. The QXRD and PC results generally agreed well for the total hematite concentration, however the QXRD results were lower than PC for magnetite and total SFCA. Some of this difference may be explained by the glass concentration, which was estimated based on the amorphous material present in the QXRD pattern. The inverse relationship between glass concentration determined from imaging and QXRD implies other additional sources for the amorphous concentration identified by XRD, particularly in the higher basicity samples. C2S content was under-reported by PC and SEM, probably due to loss of this phase during sample preparation.

Not all of the SFCA-I measured by XRD was identified on the basis of morphology during PC. It is probable that some of the SFCA-I present in the high basicity sample has a different morphology in two-dimensional section using reflected light microscopy.

The use of the SEM-based systems to distinguish SFCA and SFCA-I on the basis of chemical analysis was only partially successful, with some uncertainty due to limited resolution of data for individual point analyses and problems in direct correlation with the known relationship between SFCA (low Fe, high Si) and SFCA-I (high Fe) composition.

Automated scanning electron microscopy using the TIMA system was unable to distinguish hematite from magnetite with the setting used; however, reasonable discrimination was achieved with QEMSCAN, although the calibration was sensitive and the identification is in some cases influenced by mineral association, due to very fine intergrowth of phases. There is potential for further refinement of these techniques, in particular with detailed microprobe analysis of individual phases and/or EPMA mapping of reference sample areas.

Further work is recommended to resolve the differences between QXRD and microscopic techniques in terms of SFCA/SFCA-I discrimination, amorphous/glass concentration and overall magnetite/SFCA concentration. This work should include EPMA mapping of SFCA textures to better quantify their chemical compositions, as well as QXRD mapping. A major challenge that remains is then to improve our understanding of the relationships between sinter mineralogy and its metallurgical performance.

Author Contributions: Writing—original draft preparation was done by T.H., J.M., E.D., M.I.P. and X.L. Investigation was carried out by L.M., J.M., E.D., N.W., J.L., G.Z. and H.L. Conceptualization was performed by T.H., B.M., D.O. and D.P. All authors took part in a number of collaborative workshops during the project.

Funding: This research was funded by the Australian Research Council through the ARC Research Hub for Advanced Technologies for Australian Iron Ore and the ARC Research Hub for Australian Steel Manufacturing.

Acknowledgments: The authors acknowledge the funding of the Australian Research Council in supporting the ARC Research Hub for Advanced Technologies for Australian Iron Ore, the ARC Research Hub for Australian Steel Manufacturing and our industry partners for their financial support and permission to publish this paper. The authors acknowledge the support of BlueScope Steel, BHP and CSIRO Mineral Resources, especially Tirsha Raynlyn, Peter Austin and Mike Peterson, for carrying out optical and QEMSCAN analysis.

Conflicts of Interest: The authors declare no conflict of interest.

References

1. Cai, B.; Watanabe, T.; Kamijo, C.; Susa, M.; Hayashi, M. Comparison between reducibilities of columnar silico-ferrite of calcium and aluminum (SFCA) covered with slag and acicular SFCA with fine pores. *ISIJ Int.* **2018**, *58*, 642–651. [CrossRef]
2. Maruoka, D.; Mataoka, S.; Murakami, T.; Kasai, E. Influence of crystal structure and chemical composition of silico-ferrite of calcium and aluminum on its reducibility. In Proceedings of the 8th International Congress on Science and Technology of Ironmaking, Vienna, Austria, 25–28 September 2018; pp. 367–372.
3. Honeyands, T.; Manuel, J.; Matthews, L.; O'Dea, D.; Pinson, D.; Leedham, J.; Monaghan, B.; Li, H.; Chen, J.; Hayes, P.; et al. Characterising the mineralogy of iron ore sinters—State-of-the-art in Australia. In Proceedings of the Iron Ore 2017, Perth, Australia, 24–26 July 2017; pp. 49–60.
4. Nicol, S.; Chen, J.; Pownceby, M.; Webster, A. A review of the chemistry, structure and formation conditions of silico-ferrite of calcium and aluminum ('SFCS') phases. *ISIJ Int.* **2018**, *58*, 2157–2172. [CrossRef]
5. Mezibricky, R.; Frolichova, M. Silico-ferrite of calcium and aluminum characterization by crystal morphology in iron ore sinter microstructure. *ISIJ Int.* **2016**, *56*, 1111–1113. [CrossRef]
6. Hamilton, J.; Hoskins, B.; Mumme, W.; Borbidge, W.; Montague, M.A. The crystal structure and crystal chemistry of $Ca_{2.3}Mg_{0.8}Al_{1.5}Si_{1.1}Fe_{8.3}O_{20}$(SFCA): solid solution limits and selected phase relationships of SFCA in the SiO_2-Fe_2O_3-CaO(-Al_2O_3) system. *Neues Jahrb. Mineral. Abh.* **1989**, *161*, 1–26.
7. Mumme, W.; Clout, J.; Gable, R. The crystal structure of SFCA-I, $Ca_{3.18}Fe3^{+}{}_{14.30}Fe^{2+}{}_{0.55}O_{25}$, a homologue of the aenigmatite structure type, and new crystal structure refinements of β-CFF, $Ca_{2.99}Fe^{3+}{}_{14.30}Fe^{2+}{}_{0.55}O_{25}$ and Mg-free SFCA, $Ca_{2.45}Fe^{3+}{}_{9.04}Fe^{2+}{}_{0.16}O_{20}$. *Neues Jahrb. Mineral. Abh.* **1998**, *173*, 93–117.
8. Patrick, T.; Pownceby, M. Stability of silico-ferrite of calcium and aluminum (SFCA) in air-solid solution limits between 1240 °C and 1390 °C and phase relationships within the Fe_2O_3–CaO–Al_2O_3–SiO_2; (FCAS) system. *Metall. Mater. Trans. B* **2002**, *33*, 79–89. [CrossRef]
9. Webster, N.; Pownceby, M.; Madsen, I.; Kimpton, J. Silico-ferrite of calcium and aluminum (SFCA) iron ore sinter bonding phases: new insights into their formation during heating and cooling. *Metall. Mater. Trans. B* **2012**, *43*, 1344–1357. [CrossRef]
10. Tonzetic, I.; Dippenaar, A. An alternative to traditional iron-ore sinter phase classification. *Miner. Eng.* **2011**, *24*, 1258–1263.
11. Donskoi, E.; Poliakov, A.; Manuel, J.; Peterson, M.; Hapugoda, S. Novel developments in optical image analysis for iron ore, sinter and coke characterisation. *Appl. Earth Sci.* **2015**, *124*, 227–244. [CrossRef]
12. Donskoi, E.; Hapugoda, S.; Lu, L.; Poliakov, A.; Peterson, M.; Haileslassie, A. Advances in optical image analysis of iron ore sinter. In Proceedings of the Iron Ore 2015, Perth, Australia, 13–15 July 2015; pp. 543–548.
13. Hapugoda, S.; Lu, L.; Donskoi, E.; Manuel, J. Mineralogical quantification of iron ore sinter. *Miner. Process. Extr. Metall.* **2016**, *125*, 156–164. [CrossRef]
14. Malvern Panalytical. *X'Pert HighScore Plus*, Version 4; PANalytical B V: Almelo, The Netherlands, 2014.
15. Rietveld, H. A profile refinement method for nuclear and magnetic structures. *J. Appl. Crystallogr.* **1969**, *2*, 65–71. [CrossRef]
16. Bruker AXS. *TOPAS V5: General Profile and Structure Analysis Software for Powder Diffraction Data*; Bruker AXS: Karlsruhe, Germany, 2013.
17. Blake, R.; Hessevick, R.; Zoltai, T.; Finger, L. Refinement of the hematite structure. *Am. Min.* **1966**, *51*, 123–129.
18. Hamilton, W. Neutron diffraction investigation of the 119°K transition in magnetite. *Phys. Rev.* **1958**, *110*, 1050–1057.
19. Liles, D.C.; de Villiers, J.P.; Kahlenberg, V. Refinement of iron ore sinter phases: A silico-ferrite of calcium and aluminium (SFCA) and an Al-free SFC, and the effect on phase quantification by X-ray diffraction. *Miner. Petrol.* **2016**, *110*, 141–147. [CrossRef]
20. Tsurumi, T.; Hirano, Y.; Kato, H.; Kamiya, T.; Daimon, M. Crystal structure and hydration of belite locality: synthetic. *Ceram. Trans.* **1994**, *40*, 19–25.
21. Madsen, I.; Scarlett, N. Quantitative Phase Analysis. In *Powder Diffraction: Theory and Practice*; Royal Society of Chemistry: London, UK, 2008; pp. 298–331.
22. Goodall, W. Characterisation of mineralogy and gold deportment for complex tailings deposits using QEMSCAN. *Miner. Eng.* **2008**, *21*, 518–523. [CrossRef]

23. Hrstka, T.; Gottlieb, P.; Skala, R.; Breiter, K.; Motl, D. Automated mineralogy and petrology—Applications of TESCAN Integrated Mineral Analyzer (TIMA). *J. Geosci.* **2018**, *63*, 47–63. [CrossRef]
24. Ostwald, J. Mineralogy and microtexture of Australian iron ore sinters. *BHP Tech. Bull.* **1981**, *25*, 13–20.
25. Webster, N.; Pownceby, M.; Madsen, I.; Studer, A.; Manuel, J.; Kimpton, J. Fundamentals of Silico-ferrite of Calcium and Aluminum (SFCA) and SFCA-I Iron Ore Sinter Bonding Phase Formation: Effects of CaO:SiO_2 Ratio. *Metall. Mater. Trans. B* **2014**, *45*, 2097–2105. [CrossRef]
26. Webster, N.; Churchill, J.; Tufaile, F.; Pownceby, M.; Manuel, J.; Kimpton, J. Fundamentals of Silico-Ferrite of Calcium and Aluminum (SFCA) and SFCA-I iron ore sinter bonding phase formation: Effects of titanomagnetite-based ironsand and titanium addition. *ISIJ Int.* **2016**, *56*, 1715–1722. [CrossRef]
27. Murao, R.; Harano, T.; Kimura, M.; Jung, I. Thermodynamic modeling of the SFCA phase Ca2(Fe,Ca)6 (Fe,Al,Si)6O20. *ISIJ Int.* **2018**, *58*, 259–266. [CrossRef]
28. Webster, N.; Pownceby, M.; Madsen, I. In situ X-ray Diffraction Investigation of the Formation Mechanisms of Silico-Ferrite of Calcium and Aluminum-I-type (SFCA-I-type) Complex Calcium Ferrites. *ISIJ Int.* **2013**, *53*, 1334–1340. [CrossRef]